The University of
Nottingham

UNITED KINGDOM · CHINA · MALAYSIA

Degano, Michele and Carraro, M. and Bianchi, Nicola (2015) Selection criteria and robust optimization of a traction PM-Assisted Synchronous Reluctance motor. IEEE Transactions on Industry Applications, 51 (6). pp. 4383-4391. ISSN 1939-9367

Selection Criteria and Robust Optimization
of a Traction PMASR Motor

Michele Degano[(o)], Enrico Carraro[(x)] and Nicola Bianchi[(x)]

[(x)] Dept. of Industrial Engineering, Univ. of Padova, via Gradenigo 6/A, 35131 PD (ITALY)
[(o)] Dept. of Electrical, Electronic and Computer Engineering, Univ. of Trieste, 34127 TS (ITALY)

Abstract—In the coming years, the electrification and the deployment of the electric motors in the urban transports will become a reality more and more widespread. The optimization stage of the electric motors usually does not consider in detail the real driving conditions of the car in which the motor is installed. It follows that the actual motor performance in operating points, especially as regards the torque ripple and the efficiency, might be worsen than expected. A robust solution is a required target. This paper deals with the design and optimization of a high speed permanent magnet assisted synchronous reluctance motor for traction applications, taking into account of both city and highway driving cycles. A procedure is employed in order to evaluate the most representative operating points, which have to be considered for the global optimization. An analysis of the robustness of the solutions has been performed. Both results and advantages of the adopted methodology are highlighted.

I. INTRODUCTION

The progressive electrification of the private transport systems is becoming a well-established reality in the international scenario since it is seen as the most promising solution to reduce air pollution, oil dependency and to improve energy efficiency. As for convention internal combustion engine (ICE) vehicles, the performance of an electric vehicle are strictly related to the driving conditions of the car in which the motor is installed. On the other hand, the optimization procedure of the electric motors does not often consider the actual working conditions. For this reason, when the machine works, it becomes mandatory to optimize the design in the most profitable areas in which the motor operates, in order to improve the overall performance. On this basis, some recent researches [1]–[4] have introduced new design and optimization techniques for traction motors, in order to enhance the efficiency against a defined driving cycle. On the other hand, previous researches have investigated neither the optimization of the torque ripple, nor the robustness of the solution, over the aforementioned driving cycle.

This paper aims to present an optimization procedure of a Permanent Magnet Assisted Synchronous Reluctance (PMASR) motor for traction application, considering a city and a highway driving schedule. The motor is equipped with a 36-slot 4-pole and an integral-slot distributed winding. A high grade Ferrite PM is considered. The interest in Ferrite-based PMASR motors [5]–[8] is spreading in the last years, as a consequence of the instability and the increase of the price of rare earth magnets. Moreover, it provides a high flux weakening operating range, which is usually an important requirement in traction applications. Conversely, the most important drawback is the intrinsically higher torque ripple [9] which can be reduced by means of different strategies, such as an optimization of the shape of the flux barriers and skewing [10], [11].

This paper introduces a novel optimization strategy that takes into account both high efficiency and low torque ripple performance, analyzing the robustness of the solutions over the whole driving cycle.
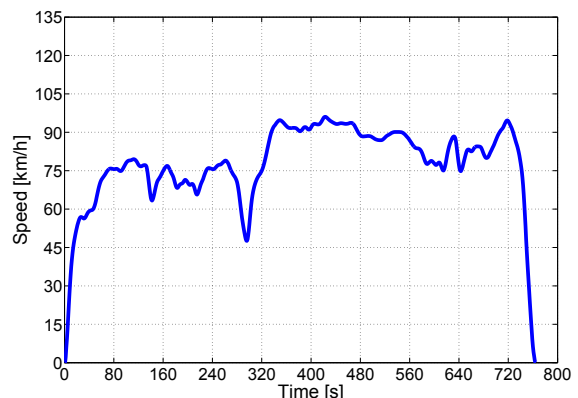
II. EVALUATION OF THE MOTOR REQUIREMENTS

A. Driving cycles

The motor performance have been assessed on the basis of two US driving cycles used to measure the fuel consumption and gas emission of light-duty vehicles.
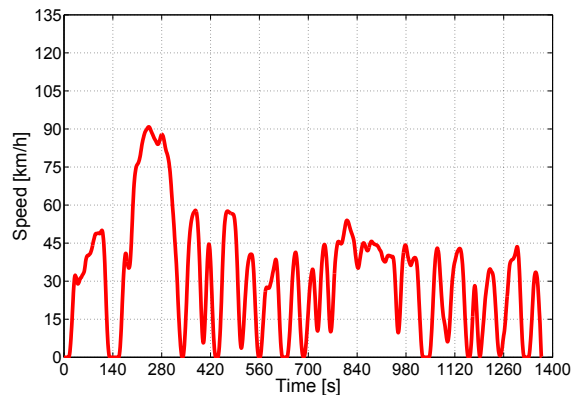
(a) UDDS

(b) HWFET

Fig. 1: Driving cycle speed vs. time profiles.

The first, the Urban Dynamometer Driving Schedule (UDDS), is reported in Fig. 1(a). It is suitable for city driving. The cycle simulates an urban route of about $12\ km$ with frequent stops with a maximum speed of about $91\ km/h$. It includes 23 stops over a period of $23\ min$ for an average speed of $32\ km/h$.

The second, the Highway Fuel Economy Driving Schedule (HWFET), is reported in Fig. 1(b). It represents the highway driving cycle. It is characterized by a no-stop operation over a route of $16\ km$, with an average speed and a top speed of $77\ km/h$ and $97\ km/h$, respectively [12].

B. Torque and power distributions

In the analysis presented in this paper these driving cycles are assumed to be performed by a medium size car with a mass of about $m = 1500\ kg$, equipped with two high speed PMASR motors. Each of them is connected to the respective wheel, with a diameter of $D_w = 500\ mm$, by means of a gearbox with a $1 : 8$ ratio. According to the method proposed in [13], the motor torque vs. speed distributions have been evaluated on the basis of the traction forces F_t computed, from the inertia force F, friction force F_f and drag force F_d, as reported in (1). The grading force has not been accounted since the route covered by the vehicle is flat.

$$\begin{cases} F_t = F + F_f + F_d & \text{(1a)} \\ F = m \cdot a & \text{(1b)} \\ F_f = 0.01 \cdot \left(1 + \dfrac{v}{44.4}\right) \cdot m \cdot g & \text{(1c)} \\ F_d = \dfrac{1}{2} \cdot c_x \cdot S \cdot v^2 & \text{(1d)} \end{cases}$$

where v is the car speed, a is the car acceleration, g is the gravitational acceleration. The frontal area and the drag coefficient, have been estimated on the basis of the average values of a typical medium size car, which are $S = 1.85\ m^2$ and $c_x = 0.4$, respectively.

The torque and power vs. speed distributions, for both the driving cycles, are reported in Fig. 2. Since the optimization has been performed in the motor operation, the regenerative working area has been neglected in the present analysis.

The target available torque and power curves are highlighted, assuming a hyperbolic trend over the base speed such as to ensure an ideal constant power speed range. The motor has to develop a rated torque of about $33\ Nm$ up to the base speed of about $4000\ rpm$, with a maximum speed in the order of $8000\ rpm$.

It is worth noticing that, for both the driving cycles, the machine operates mainly at low torque. The RMS torque, that provides an assessment of the thermal state of the machine, is about $11\ Nm$ for the UDDS and $9\ Nm$ for the HWFET. It follows that, even if the motor has to be designed for the rated torque, the optimization have to be effectively addressed in low torque operation.

Two representative operating torque-speed points, the first for the city, the second for the highway driving, have been computed. These points, in which the machine works for most
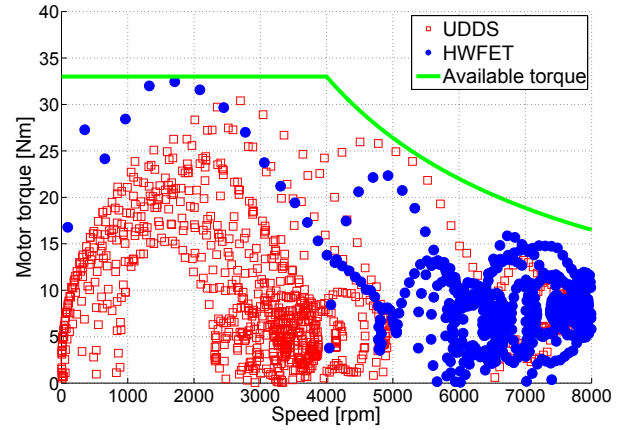
(a) Torque vs. speed.
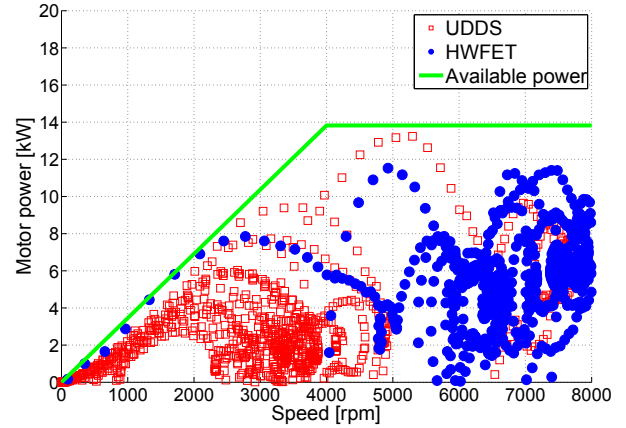
(b) Power vs. speed.

Fig. 2: Electromechanical characteristics.

of the duration of the driving cycle, are $5\ Nm$ at $3500\ rpm$ for the UDDS and $7.5\ Nm$ at $7000\ rpm$ for the HWFET.

III. DESIGN AND OPTIMIZATION

A 36-slot 4-pole PMASR, integral slot distributed winding design, has been considered. The main motor dimensions are based on an existing prototype [14], reported in Fig. 3(a) and designed and optimized for an automotive application. The outer and airgap diameter are $200\ mm$ and $125\ mm$ respectively, while the airgap height is equal to $0.35\ mm$. The prototype has been manufactured and tested. As shown in [14], a good agreement between the experimental results and Finite Element Analysis (FEA) is achieved.

As reported in Table I, the city and highway operating points, evaluated in II-B, correspond to specific space current vectors and frequencies. As shown in Fig. 3(c) the city driving point is located along the maximum torque per ampere locus, while the HWFET is in Flux Weakening (FW) working point. In both UDDS and HWFET operating points the optimization has been set to minimize the torque ripple T_r and the losses P_l, (2a-2d). On the basis of the aforementioned stator lamination and the requested motor specification, a new optimized design has been evaluated. The machine has been designed in order to meet the target torque and power profile ensuring a safe

TABLE I: Representative operating points of the driving cycles.

Name	Symbol	UDDS	HWFET	Unit
Torque	T	5	7.5	Nm
Speed	n	3500	7000	rpm
Current density	J	2.2	3	A_{RMS}/mm^2
Current angle	α_{ie}	53	73	$degrees$
Frequency	f	116	233	Hz

demagnetization at the operating temperature in the range between 150 °C and 180 °C, working at a rated current density of about 9 A/mm^2. The stack length and the number of conductors have been adjusted to meet different rated torque specifications and providing a base speed around the target value of 4000 rpm. An optimization algorithm has been performed to the aim of minimizing torque ripple T_r and losses P_l.

Furthermore, an evaluation and optimization of the robustness of the machine has been carried out. The robustness is a concept complementary to the sensitivity. A robust machine is defined as that machine configuration that exhibits the minimum sensitivity to any variation of the system parameters [15]–[17], that is, to any dimensional or operational (working conditions) variation. As reported in (2e) and (2f), the machine has to exhibit low torque ripple and losses. This is checked by imposing comparable performance as regards the torque ripple and losses in both operating conditions. Thus, the performance difference ΔT_r and ΔP_l, has to be minimized.

The objective functions are defined as:

$$\begin{cases} min(T_{rUDDS}) & \text{(2a)} \\ min(T_{rHWFET}) & \text{(2b)} \\ min(P_{lUDDS}) & \text{(2c)} \\ min(P_{lHWFET}) & \text{(2d)} \\ min(\Delta T_r) = min|T_{rUDDS} - T_{rHWFET}| & \text{(2e)} \\ min(\Delta P_l) = min|P_{lUDDS} - P_{lHWFET}| & \text{(2f)} \end{cases}$$

Before selecting the optimization variables, it is important to consider their influence with respect to the objective functions. The sketch in Fig. 4 shows the main geometrical parameters that have been considered for the current study of this PMASR motor.

The airgap, inner and outer stator diameters, D, D_r and D_e respectively, together with the electric loading have been kept as geometry constraints, thus ensuring a limited variation of the torque along the operation trajectory. It is well known that the motor performance are influenced by several parameters, since PMASR motors have intrinsically many degrees of freedom (especially the rotor geometry).

The torque ripple is determined by the interaction between the spatial harmonics of magneto-motive force (MMF) due to the stator currents and the rotor geometry and it is one of the main drawbacks of these motors. In [17] it has been shown that the torque ripple is very sensitive to the geometry along the airgap region. For instance, there is a strong impact of the angles of the flux barrier ends (i.e. θ_{b1}, θ_{b2}, θ_{b3} of Fig. 4 assuming a rotor with three flux barriers per pole).
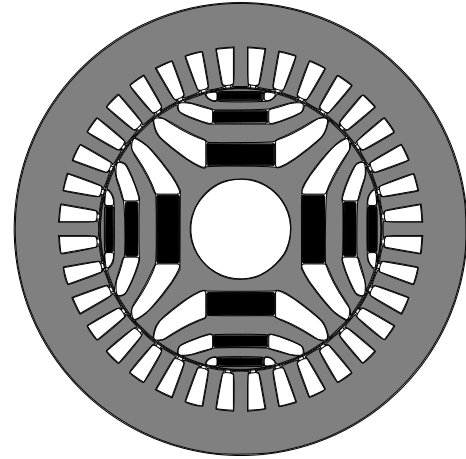
(a) PMASR motor cross section.
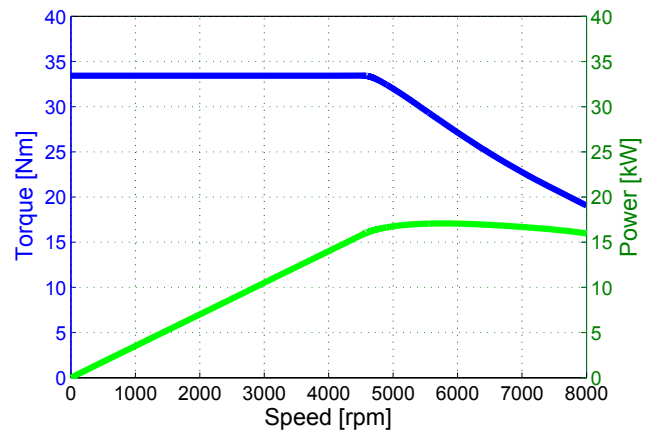
(b) Motor torque and power vs. speed characteristics. Current vector follows the MTPA and FW trajectories.
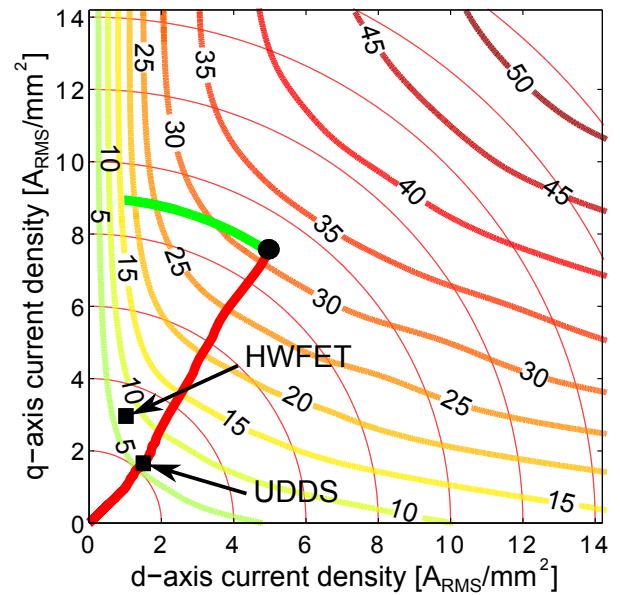
(c) J_d-J_q Current Density plane

Fig. 3: Operation trajectory and representative operating points of the PMASR motor prototype, in the J_d-J_q plane. Constant current and constant curves are reported.
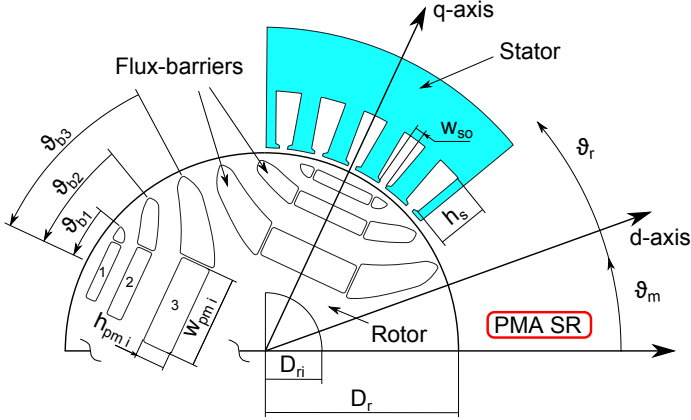
Fig. 4: PMASR geometrical variables.

Name	Symbol	Boundaries		Unit
		Lower	Upper	
Flux barrier angle 1	θ_{b1}	13	16	$degrees$
Flux barrier angle 2	θ_{b2}	25	28	$degrees$
Flux barrier angle 3	θ_{b3}	38	40	$degrees$
Insulation coefficient	k_{air}	0.35	0.45	–
Slot opening	w_{so}	1	4	mm
Slot height	h_s	12	22	mm
Tooth width	w_t	4	8	mm

A. Optimization procedure

Fig. 9 shows a scheme of the optimization steps.

Fig. 5: Optimization Process flow chart with MOGA-II.

Other influent parameters are the slot opening width w_{so} and the iron bridges height (also called iron ribs) h_{rib}. The first is suitable to be optimized, even if there is a minimum threshold to be considered, depending on the diameter of the elementary conductor that has to be placed into the stator slot. The second parameter has to be designed with respect to the mechanical stress due to the mechanical forces arising at high rotational speed.

Regarding the thickness of the flux barriers and the permanent magnet dimensions, some considerations can be done. The portion of air (or PMs) with respect to the iron along the q-axis, is defined as insulation coefficient. This parameter is defined as follows:

$$k_{air} = \frac{2 \cdot \sum_i h_{pmi}}{D_r - D_{ri}} \tag{3}$$

where h_{pmi} is the PM thickness of the i-th flux barrier, D_r is the rotor diameter, D_{ri} is the shaft diameter. The choice of k_{air} is strongly related with two main design specifications. The first is the iron saturation level in the machine, whose effect has been deeply investigated in [14]. The second is the high saliency ratio ξ, in order to guarantee a proper reluctance torque.

Conversely, PM dimensions have to be chosen taking into account the demagnetization, which can occur when the machine is working in deep flux weakening condition (high speed). Let us remember that the main role of the PMs in this type of motors is to saturate the iron bridges as well as enhance the power factor.

For this reasons, in order to explore the effect of the most influent parameters of both rotor and stator of the PMASR under study, the selected optimization variables are:

- the flux barriers end angles θ_{b1}, θ_{b2}, θ_{b3},
- the insulation coefficient k_{air},
- the slot opening w_{so},
- the slot height h_s,
- the tooth width w_t.

Table II reports the range of variation of these optimization variables.

The number of individuals N in the design of experiments table, are used as the initial population. The sequence of initial individuals has been determined using a pseudo random Sobol criteria. The Sobol method creates sequences of n-tuples that fill the n-dimensional design space more uniformly than a random sequence. The purpose of this work, apart from satisfying the objective function constraints, it is also to achieve an explorative optimization over all the parameters space. This allows to find out possible local minima. Thus, the experiments are uniformly distributed in the design space.

Once the input motor variables are set, an automatic and parametric procedure is carried out. The geometry is automatically drawn. Sources and boundary conditions are set. Field solution is found in various rotor positions. The FEA results are then post-processed in order to determine the torque ripple and the motor losses for both UDDS and HWFET working points.

The optimization algorithm MOGA-II has been chosen with the aim of achieving a fast Pareto convergence. It is based on Multi Objective Genetic Algorithm (MOGA) and works on a set of design configurations which are periodically updated when one generation is completed. The algorithm type is a generational evolution. MOGA-II is an efficient multi-objective genetic algorithm that uses a smart multi-search elitism. The concept of elitism enhances the convergence properties towards the Pareto-optimal set. This operator is

able to preserve some solutions without bringing premature convergence to local-optimal frontiers. These are the closest to the Pareto front exhibiting the best dispersion. Elitism is introduced storing all non-dominated solutions discovered so far, including the initial population.

The operators of crossover, mutation and selection have been set in order to provide robustness and efficiency to the optimizer. At each step of the reproduction process, one operator is chosen and applied to each individual. A new set of variables, selected among the boundaries reported in Table II, is then reassigned and the FEA is carried out again for the next generation.

B. Evaluation of the robustness

As mentioned in the previous section, the robustness concept has been introduced as an objective function of the optimization procedure. In order to evaluate quantitatively the robustness of the solutions of the final Pareto front a general mathematical procedure is presented hereafter.
Even this method can be easily extend to a hyperspace, two objective functions y_1 and y_2 in the bidimensional space are considered in this analysis. They are reported in Fig. 6.
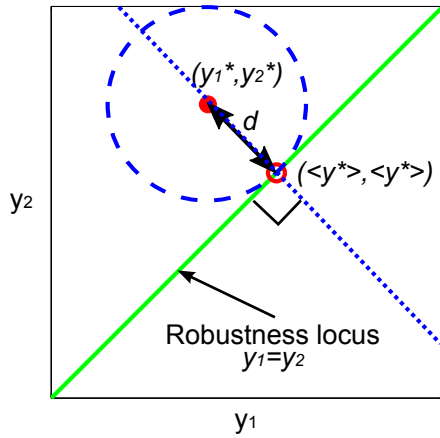

Fig. 6: Concept of the robustness for a 2 - objective functions design space.

The solutions which show the same value of the objective function $y_1^* = y_2^*$ are the most robust in the Pareto front. Thus, a robustness locus exists and it is described by a linear relationship $y_2 = y_1$. Considering the general solution (y_1^*, y_2^*) in the design space, a representative distance of this combination to the robustness curve is evaluated along the perpendicular line between the point (y_1^*, y_2^*) and the line $y_2 = y_1$. As shown in (5), the intersection point coordinate ($< y^* >$, $< y^* >$) is equal to the mean value of the two objective functions:

$$< y^* > = \frac{y_1^* + y_2^*}{2} \qquad (4)$$

Every solution that exhibits the same mean value lies on the same straight line perpendicular to the robustness locus. The distance of the solution (y_1^*, y_2^*) to the intersection point ($< y^* >$, $< y^* >$) is defined as,

$$d = \sqrt{(y_1^* - < y^* >)^2 + (y_2^* - < y^* >)^2} \qquad (5)$$

As a consequence, among the solutions exhibiting the same mean value, i.e. lying on the same straight line perpendicular to the robustness locus, the most robust solution results to be that showing the lowest distance d from the mean value.

(a) Torque ripple trend.
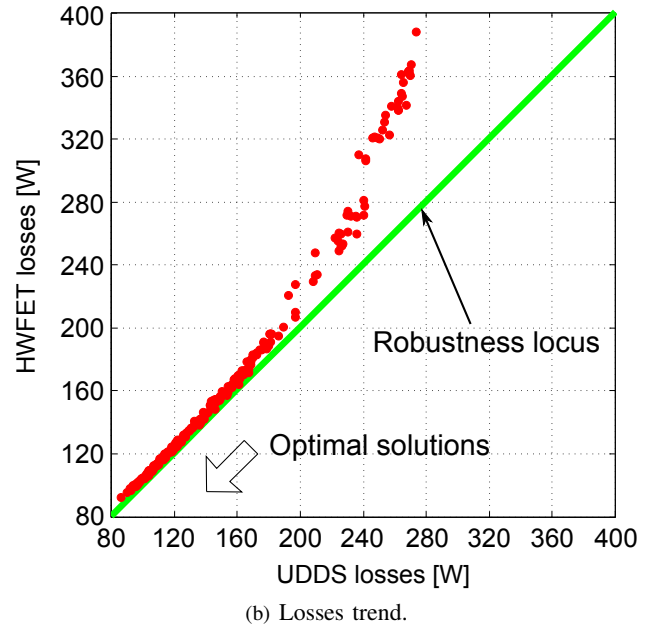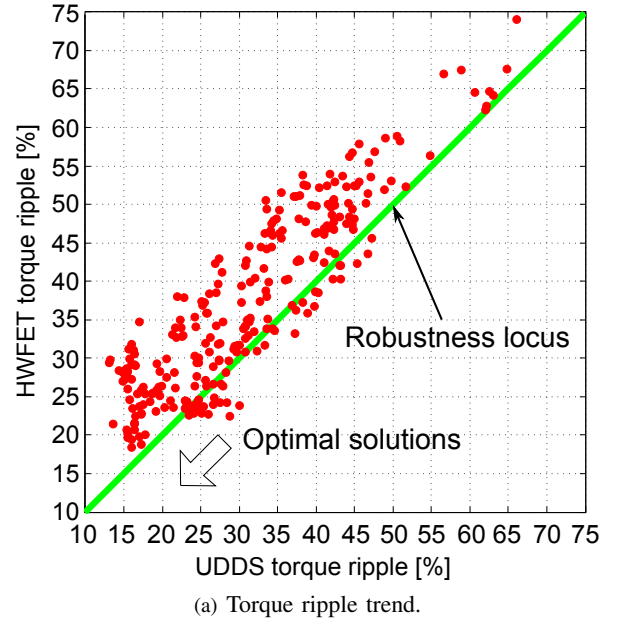

(b) Losses trend.

Fig. 7: Torque ripple and losses distributions in UDDS and HWFET cycles.

C. Results

Fig. 7 reports, for each iteration, the value of the torque ripple and the losses corresponding to the UDDS and HWFET operating points. Since the optimization procedure is aimed to find a robust design, the distribution of the points are concentrated around the robustness curves.

As shown in Fig. 7(a), the torque ripple distribution exhibits a high variation, in particular in the region above the robustness locus. The reason of this effect is mainly due to the higher torque ripple in flux weakening operation [18], i.e. in the HWFET point.

It is worth noticing that the average distance, between the solutions and the robustness locus, is quite high. This confirms that torque ripple is very sensitive to the geometrical parameters variation.

Similarly to the torque ripple, Fig. 7(b) reports the losses distribution. In this case the optimization results are more concentrated along the robustness locus. The solutions are shifted above for all cases due to the higher contribution of the iron losses at the higher speed (HWFET operating point) with respect to the UDDS point. Finally, the losses distribution diverges gradually from the robustness locus once the power loss exceeds $200\ W$. For lower values, the distance d is low, showing that losses are less sensitive to the geometrical variation within the range of variables.

Fig. 8 shows the trend of the solution distance with respect to the robustness locus vs. the mean torque ripple Fig. 8(a) and the losses Fig. 8(b). The differences are evaluated comparing UDDS and HWFET operating points, according to the concept introduced in Sec. III-B.

In Fig. 8(a), the most representative robust designs for the torque ripple are highlighted with blue filled circles, between A and B. These points exhibit the highest robustness, since the distance d from the robustness locus is approximately zero, while the mean torque ripple, in UDDS-HWFET operation, increases from A to B. Always referring to Fig. 8(a), the solution C is also considered. It exhibits a mean torque ripple lower than 20% and the lower distance d from the robustness curve.

The corresponding losses are highlighted in Fig. 8(b). It is worth noticing that the robust designs for the torque ripple do not correspond to the robust solutions as far as the losses are concerned. For istance, the solution A, which is robust in terms of torque ripple, shows a noticeable distance from the robustness losses curve (see Fig. 8(b)), while the B exhibits good robustness for both torque ripple and losses.

In order to help in the optimal solution selection, Fig. 9 reports the mean torque and losses trends of the most robust solutions ($d \simeq 0$) which, from the torque ripple point of view, are highlighted in Fig. 8(a). This representation confirms that a solution with a robustness satisfying one of the two objective functions, for instance solution A, does not necessarily satisfy the other one.

As usual, the selection of the best solution is a tradeoff between the results that better satisfy all the objective functions. In this case, considering these motor topologies and the application, the best compromise among the losses variation is resulting in design C, which is robust and exhibits low torque ripple and losses for both the considered driving cycles. In Tab. III are reported the dimensional parameters for machines A, B and C, which are sketched in Fig. 10.

Analysing more in detail the machines resulting from the optimization and represented in Fig. 8(a), it is worth noticing that there is a set of solutions, which are not the most robust
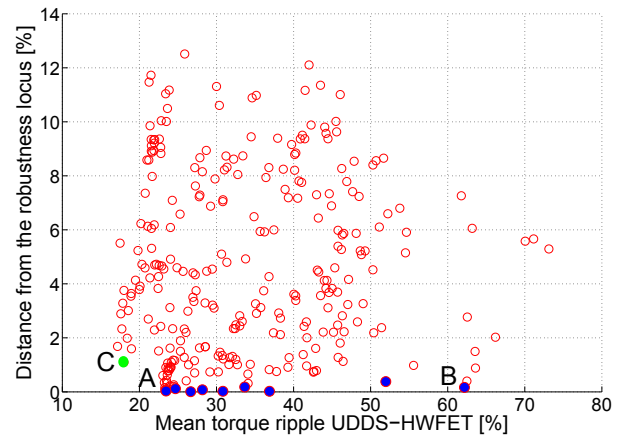
(a) Torque ripple trend.
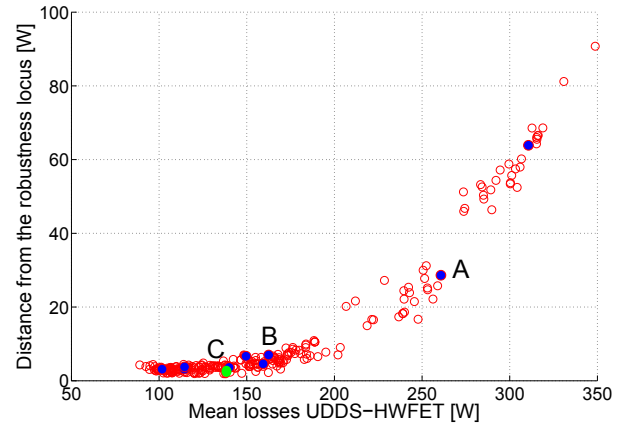
(b) Losses trend.

Fig. 8: Distance of the solution from the robustness locus in UDDS and HWFET cycles.

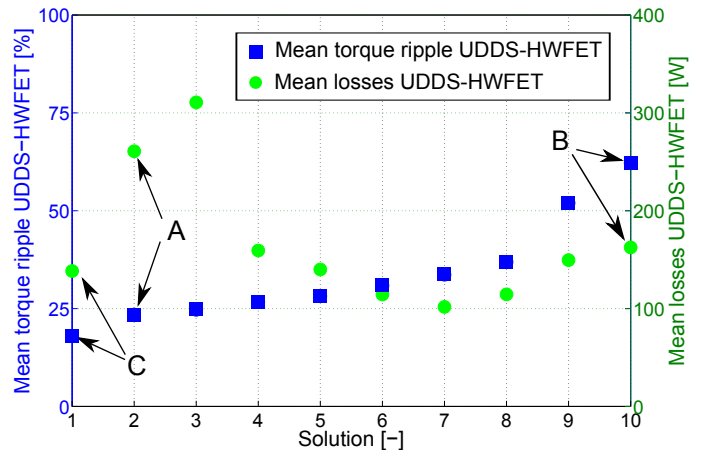Fig. 9: Mean torque ripple (blue squares) and losses (green circles) trend of the most robust solutions ($d \simeq 0\%$).

under the definition espressed by eq. 5, presenting a mean torque ripple lower than 20%.

Depending on the application and the requirements it is possible to consider solutions in a wider range of robustness, for instance the ones with d lower than 4%. In this case, similarly
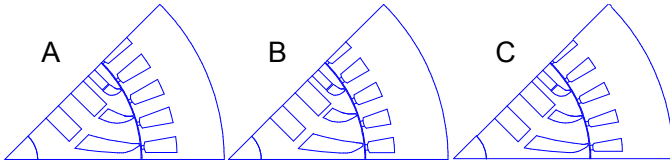
Fig. 10: Motors A, B and C.

TABLE III: Robust machines.

Name	Symbol	A	B	C	Unit
Flux barrier angle 1	θ_{b1}	13.9	13.9	14.5	*degrees*
Flux barrier angle 2	θ_{b2}	26.7	25.6	26.5	*degrees*
Flux barrier angle 3	θ_{b3}	38.7	38.7	38.6	*degrees*
Insulation coefficient	k_{air}	0.39	0.41	0.35	−
Slot opening	w_{so}	1.6	2.5	2.1	*mm*
Slot height	h_s	16	13.2	14.4	*mm*
Tooth width	w_t	6.4	6.2	7.6	*mm*

to the representation of Fig. 9, the machines performances are shown in Fig. 11. Always considering the enlargement at the bottom of Fig. 11, the motors highlighted with filled triangles are exhibiting a mean torque ripple lower than 20%. All these machines have a lower torque ripple in UDDS with respect to HWFET operating points.
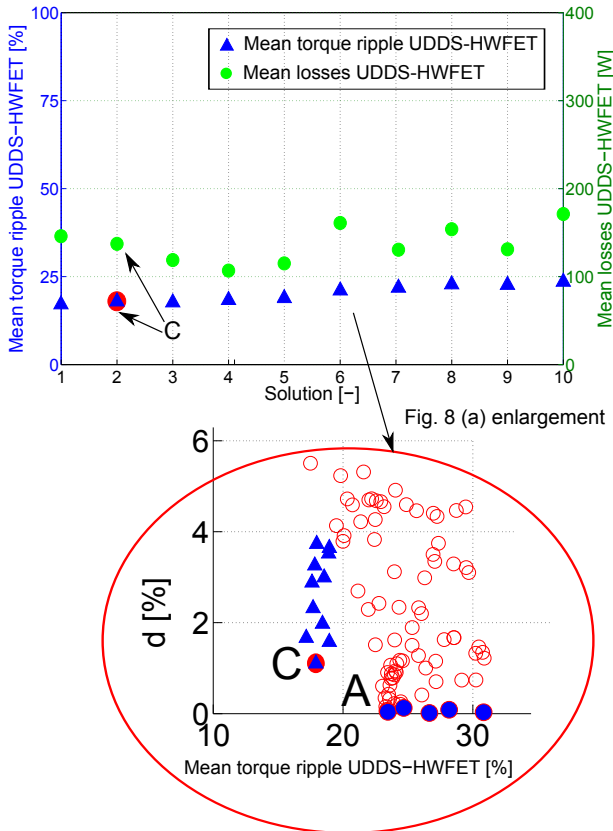

Fig. 11: *Top*: Mean torque ripple (blue triangles) and losses (green circles) trend of the solutions considering a robustness range with $d < 4\%$); *Bottom*: Enlargement with machines presenting a torque ripple lower than 20% (blue triangles).

IV. CONCLUSIONS

To the aim of designing a PMASR motor for traction application, different driving cycles have to be considered. In this paper, two driving cycles are taken into account, the first for the city driving USSD and the second for the highway driving HWFET. The electromechanical specification and the most profitable working areas have been predicted. The analysis of the geometrical parameters to be considered as optimization inputs has been done to this purpose.

The design has been optimized by means of MOGA-II genetic algorithm aimed to the minimization of the torque ripple and the losses in the considered driving cycles. The robustness concept has been defined in order to find the best solution in the design space.

It has been shown that the difference between torque ripple and losses can be introduced as additional objective functions. It is demonstrated that this help in the selection of a machine among the others, when presenting comparable performance for the two representative working points.

The analysis of the optimized solutions emphasizes that a robust solution for the torque ripple could be not a robust solution with respect to the losses. The best candidate has been selected as a tradeoff between the lower torque ripple and the most robust results. This method is suitable for the analysis over a wider range of representative points where the motor normally operates during a driving cycle.

REFERENCES

[1] P. Lazari, J. Wang, and L. Chen, "A computationally efficient design technique for electric vehicle traction machines," *IEEE Transactions on Industry Applications*, vol. PP, no. 99, pp. 1–1, 2014.

[2] L. Chen, J. Wang, P. Lombard, P. Lazari, and V. Leconte, "Design optimisation of permanent magnet assisted synchronous reluctance machines for electric vehicle applications," in *20th International Conference on Electrical Machines (ICEM)*, Sept 2012, pp. 2647–2653.

[3] L. Chen, J. Wang, P. Lazari, and X. Chen, "Optimizations of a permanent magnet machine targeting different driving cycles for electric vehicles," in *IEEE International Electric Machines Drives Conference (IEMDC)*, May 2013, pp. 855–862.

[4] E. Carraro, M. Morandin, and N. Bianchi, "Optimization of a traction PMASR motor according to a given driving cycle," in *IEEE Transportation Electrification Conference and Exposition (ITEC)*, 2014.

[5] E. Armando, P. Guglielmi, M. Pastorelli, G. Pellegrino, and A. Vagati, "Performance of IPM-PMASR motors with ferrite injection for home appliance washing machine," in *IEEE Industry Applications Society Annual Meeting (IAS)*, 2008, pp. 1–6.

[6] S. Chino, S. Ogasawara, T. Miura, A. Chiba, M. Takemoto, and N. Hoshi, "Fundamental characteristics of a ferrite permanent magnet axial gap motor with segmented rotor structure for the hybrid electric vehicle," in *IEEE Energy Conversion Congress and Exposition (ECCE)*, 2011, pp. 2805–2811.

[7] A. Vagati, B. Boazzo, P. Guglielmi, and G. Pellegrino, "Ferrite assisted synchronous reluctance machines: A general approach," in *20th International Conference on Electrical Machines (ICEM)*, 2012, pp. 1315–1321.

[8] M. Barcaro and N. Bianchi, "Interior PM machines using ferrite to substitute rare-earth surface pm machines," in *20th International Conference on Electrical Machines (ICEM)*, 2012, pp. 1339–1345.

[9] A. Fratta, G. Troglia, A. Vagati, and F. Villata, "Evaluation of torque ripple in high performance synchronous reluctance machines," in *Conference Record of the IEEE Industry Applications Society Annual Meeting*, 1993, pp. 163–170 vol.1.

[10] N. Bianchi, *Industrial Electronics Handbooks, Power Electronics and Motor Drives, 2nd edition*. CRC Press, 2011, ch. Permanent Magnet Synchronous Motors, pp. 6.1–6.35.

[11] A. Vagati, M. Pastorelli, G. Francheschini, and S. Petrache, "Design of low-torque-ripple synchronous reluctance motors," *IEEE Transactions on Industry Applications*, vol. 34, no. 4, pp. 758–765, 1998.

[12] United States Environmental Protection Agency (USEPA). [Online]. Available: http://www.epa.gov/nvfel/testing/dynamometer.htm

[13] M. Ehsani, Y. Gao, and A. Emadi, *Modern electric, hybrid electric, and fuel cell vehicles : fundamentals, theory, and design*. CRC Press, 2010, ch. Fundamentals of Vehicle Propulsion and Brake, Ch. 2, pp. 21–65.

[14] M. Ferrari, N. Bianchi, and E. Fornasiero, "Rotor saturation impact in synchronous reluctance and PM assisted reluctance motors," in *IEEE Energy Conversion Congress and Exposition (ECCE)*, 2013, pp. 1235–1242.

[15] S. Brisset, F. Gillon, S. Vivier, and P. Brochet, "Optimization with experimental design: an approach using Taguchi's methodology and finite element simulations," *IEEE Transactions on Magnetics*, vol. 37,

no. 5, pp. 3530–3533, Sep 2001.

[16] A. Omekanda, "Robust torque and torque-per-inertia optimization of a switched reluctance motor using the Taguchi methods," *IEEE Transactions on Industry Applications*, vol. 42, no. 2, pp. 473–478, March 2006.

[17] N. Bianchi, M. Degano, and E. Fornasiero, "Sensitivity analysis of torque ripple reduction of synchronous reluctance and interior PM motors," in *IEEE Energy Conversion Congress and Exposition (ECCE)*, Sept 2013, pp. 1842–1849.

[18] T. Jahns, "Flux-weakening regime operation of an interior permanent-magnet synchronous motor drive," *IEEE Transactions on Industry Applications*, vol. IA-23, no. 4, pp. 681–689, 1987.